PROCEEDINGS OF SCIENCE

Understanding the anisotropy of cosmic rays at TeV and PeV energies

Robert Rettig, Martin Pohl*
Institute of Physics and Astronomy, University of Potsdam, Karl-Liebknecht-Strasse 24/25, 14476 Potsdam, Germany
DESY, Platanenallee 6, 15738 Zeuthen, Germany
E-mail: robert.rettig@uni-potsdam.de, martin.pohl@desy.de

The anisotropy in cosmic-ray arrival directions in the TeV-PeV energy range shows both large and small-scale structures. While the large-scale anisotropy may arise from diffusive propagation of cosmic rays, the origin of the small-scale structures remains unclear. We perform three-dimensional Monte-Carlo test-particle simulations, in which the particles propagate in both magnetostatic and electromagnetic turbulence derived from a three-dimensional isotropic power spectrum. However, in contrast to earlier studies, we do not use a backtracking method for the computation of the particle trajectories, and hence anisotropy must build up from a large-scale isotropic boundary condition. It has been recently argued that the turbulent magnetic field itself generates the small-scale structures of the anisotropy if a global cosmic-ray dipole moment is present. We show that small-scale anisotropy arises even for isotropic turbulence models and homogeneous boundary conditions. We emphasize the role of escape in shaping cosmic-ray anisotropy.

The 34th International Cosmic Ray Conference,
30 July- 6 August, 2015
The Hague, The Netherlands

*Speaker.

PoS(ICRC2015)451

1. Introduction

In the last years, several observatories, such as Tibet-III [1, 2], Super-Kamiokande [3], MILAGRO [4, 5], EAS-TOP [6], ARGO-YBJ [7], HAWC [8], as well as IceCube [9, 10, 16] have detected a statistically significant anisotropy in the arrival distribution of cosmic rays at multi-TeV energies. A large-scale dipole anisotropy is usually interpreted as result of an inhomogeneous source distribution (see e.g. [11, 12, 13, 14, 15]). More difficult to explain are smaller features on angular scales $10^\circ - 30^\circ$ that were significantly detected as well. Furthermore, the anisotropy appears to be energy-dependent [6, 16] and still persists in the PeV-energy range [17].

Earlier studies of the small-scale anisotropy focus on nearby supernovae [18], the local interstellar magnetic-field structure [19], and cosmic-ray scattering off anisotropic magnetic turbulence [20]. Cosmic-ray acceleration from magnetic reconnection in the magnetotail [21] and the interaction between the heliosphere and the local interstellar magnetic field [22] have been proposed as well.

Recent theoretical studies suggest that propagation trough a turbulent magnetic field can turn an initial dipole into small-scale anisotropy. Numerically backtracking cosmic-ray trajectories from the observer through isotropic turbulence to the boundary of an outer sphere, one observes anisotropy on various scales [23]. Liouville's theorem mandates that the total power spectrum of the spherical harmonics must be conserved, thus allowing the development of higher multipole moments corresponding to smaller features in the anisotropy [24].

Cosmic-ray propagation in the Galaxy is controlled by energy-dependent escape, though, which Liouville's theorem does not account for. Likewise, escape provides for a time arrow, leading to doubts about the reliability of the backtracking methods.

We therefore investigate the arrival distribution of cosmic rays on Earth using a forward-tracking method to compute the particle trajectories. This method allows us to include particle escape and to investigate its impact on the cosmic-ray anisotropy.

2. Numerical method

We consider only non-oscillatory turbulent magnetic fields without homogeneous component. Hence, electric fields are absent, and the equation of motion reduces to

$$\frac{\mathrm{d}}{\mathrm{d}t}(\gamma m\mathbf{v}) = \frac{q}{c}\mathbf{v}\times\delta\mathbf{B}(\mathbf{r}) \,, \tag{2.1}$$

where c denotes the speed of light, γ the Lorentz factor, m the mass, q the charge, $\mathbf{r}$ the position and $\mathbf{v}$ the velocity of the cosmic-ray particle. Here, the turbulent magnetic field $\delta\mathbf{B}(\mathbf{r})$ is obtained by superposition of plane waves with random propagation direction and polarization [25, 26, 27],

$$\delta\mathbf{B}(\mathbf{r}) = \sqrt{2}\sum_{n=1}^{N}\widehat{\xi}_{\mathbf{n}}^{\mathbf{B}}A(k_n)\cos[k_n z_n' + \beta_n] \,, \tag{2.2}$$

where $\beta_n \in [0;2\pi]$ denotes the phase, $\widehat{\xi}_{\mathbf{n}}^{\mathbf{B}}$ the polarization vector of the n-th wavemode, whereas z_n' is a pathlength coordinate along the propagation direction of the n-th wavemode. The amplitude

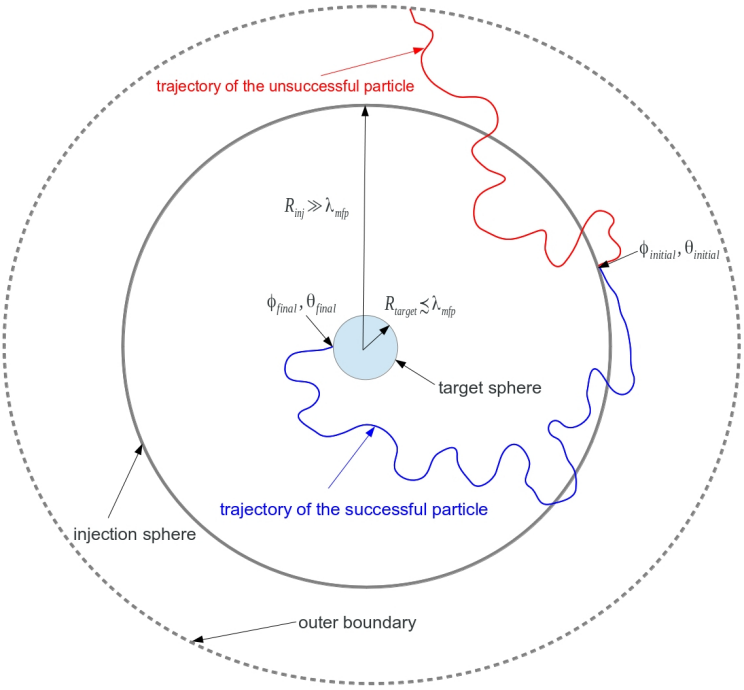

Figure 1: Sketch of the simulation setup. Particles are isotropically launched on the surface of the injection sphere and may escape when reaching the outer boundary. The arrival direction of particles hitting the target sphere in the center is recorded and used to compute the anisotropy.

$A(k_n)$ follows a Kolmogorov-type spectrum normalized to $\sqrt{\langle \delta B^2 \rangle}$ [26],

$$A^2(k_n) = \frac{\langle \delta B^2 \rangle 4\pi k_n^2 \Delta k_n}{1+(k_n L_c)^{11/3}} \left[\sum_{\nu=1}^{N} \frac{4\pi k_\nu^2 \Delta k_\nu}{1+(k_\nu L_c)^{11/3}} \right]^{-1} , \tag{2.3}$$

where the waves are assumed to be logarithmically spaced, yielding a constant ratio $\Delta k_n / k_n$. Phase, polarization, and direction of each wave are randomly chosen, thus forming a "field realization". Test simulations suggest that already $N = 50$ wavemodes are sufficient and a reasonable compromise between computational effort and numerical accuracy.

The equation of motion (2.1) is numerically integrated using a finite-difference scheme. We assume a parabolic trajectory within each time interval, Δt, which permits accurate sampling of the magnetic acceleration without requiring that the pathlength per timestep be much small than the smallest wavelength, $\lambda_{\rm min}$, of the magnetic-turbulence spectrum.

As sketched in Figure 1, the simulation volume is spherical with radius $R_{\rm bound}$, and we define Earth to be located at the center position $\mathbf{r} = 0$. As particles hit the target only by chance, we limit the computational expense by not treating our target as a point in space, but rather as a sphere with radius $R_{\rm target}$. We launch test particles with random momentum directions at randomly chosen positions on the surface of a second sphere, whose volume is much larger than that of the target sphere, implying $R_{\rm inj} \gg R_{\rm target}$, but $R_{\rm bound} \gg R_{\rm inj}$. The latter condition permits treating the outer boundary of the simulation volume as escape boundary. If a particle crosses the outer boundary at $R_{\rm bound}$, integration of its equation of motion is aborted and restarted with a new initial position and momentum direction until the particle successfully hits the target sphere. The propagation process of the particles may be truncated too early, if the outer boundary is not sufficiently far away from the injection sphere. A good compromise between reliable results and computational

	R [PV]	$\lambda_{\rm max}$ [10 pc]	$B_{\rm rms}$ [μG]	P	$\lambda_{\rm mfp}$ [pc]	$R_{\rm target}$ [pc]	$R_{\rm inj}$ [10 pc]	$R_{\rm bound}$ [10 pc]	F [%]
case 1	1	0.1	3	11.3	4.0	1.0 (0.5)	5	10	4.3 (8.5)
case 2	1	1	3	1.1	0.9	0.9 (0.45)	2.5	5	2.7 (4.9)
case 3	1	10	3	0.1	1.9	1.0 (0.5)	2.5	5.5	2.7 (4.8)
case 4	1	100	3	0.01	9.7	1.0 (0.5)	5	11	7.9 (14.9)

Table 1: Parameters used in the test-particle simulations. The rigidity of the particle, R, and the strength of the turbulent magnetic field, $B_{\rm rms}$, define the scaling to physical values of $\lambda_{\rm mfp}$, and together with $\lambda_{\rm max}$ also the physical radii of the target and injection spheres and the outer boundary. The parameter P encodes the value of the Larmor radius. The values in the brackets correspond to those of a target sphere with radius halved, and F denotes the statistical uncertainty per pixel in the final intensity distribution.

effort is found, if the mean propagation time of the particles hitting the target sphere is comparable to that of the particles crossing the outer boundary.

Charged particles experience scattering in the turbulent magnetic field, giving rise to spatial diffusion with a scattering mean free path, $\lambda_{\rm mfp}$, which can be obtained along with the diffusion coefficient

$$D = \frac{\langle (\Delta r)^2 \rangle}{6t} = \lambda_{\rm mfp} \frac{c}{3} \tag{2.4}$$

of an ensemble of ultrarelativistic particles. Here, the mean square displacement, $\langle (\Delta r)^2 \rangle$, is deduced from the particle trajectories in test-particle simulations. To obtain reliable results we require that the radius of the target sphere be smaller than, or at most comparable to, the scattering mean free path, $R_{\rm target} \leq \lambda_{\rm mfp}$. To check whether the choice of the size of the target sphere affects the results, we also consider a smaller target sphere with radius halved.

The mean free path must always be much smaller than the typical propagation length of simulated particles, $\lambda_{\rm mfp} \ll R_{\rm inj}$ to guarantee that the particle ensemble propagates long enough to sample a sufficiently large part of the turbulent magnetic field and to deeply enter the diffusive regime. We check the reliability of our results by testing larger propagation volumes and changing the radius of the injection sphere.

After crossing the surface of the target sphere, we stop tracking the trajectories and convert the final momentum directions of the particles into spherical coordinates. The subsequent representation of the arrival direction is performed using the 768-pixel *HEALPix* scheme, corresponding to an angular resolution of 7.33° [28].

3. Results

The simulation itself is dimensionless, as all lengths can be scaled to the Larmor radius of a particle in the turbulent magnetic field, $r_{\rm L} = R/B_{\rm rms}$, where the rigidity of the charged particle, R, and the rms strength of the magnetic turbulence, $B_{\rm rms} = \sqrt{\langle \delta B^2 \rangle}$, also define the gyroperiod, $\Omega^{-1} = R/cB_{\rm rms}$, as a characteristic time scale of particle motion.

In all cases, the smallest wavelength of the magnetic-turbulence spectrum, $\lambda_{\rm min}$, is much smaller than any other characteristic length in the system. We do explore different values for

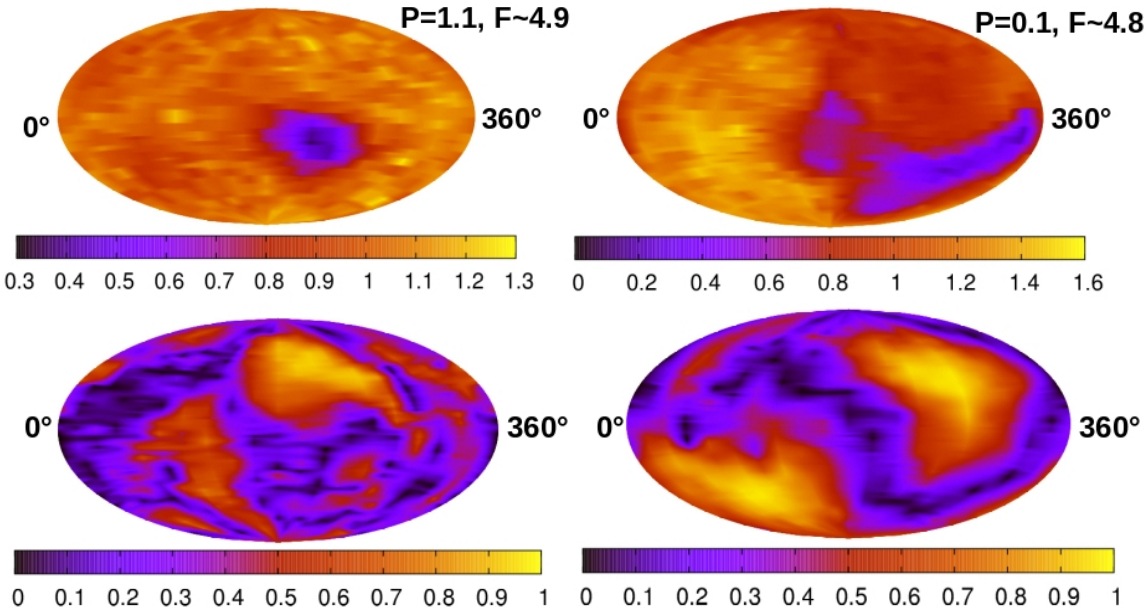

Figure 2: *Top panel:* Arrival distributions of the particle ensemble for a specific realization of the turbulent magnetic field and a small target sphere of about 0.5 pc radius, represented as relative intensities $I_{\rm pixel}/I_0$ of the appropriate fluxes. *Bottom panel:* Average magnetic-field direction in the vicinity of the target sphere, expressed as mean $\cos\theta$ between the line of sight and the magnetic field over 1–6 target radii. Values close to unity indicate a predominantly radial field. In both rows, the left panels are for case 2, and the right panels correspond to case 3.

the largest wavelength, $\lambda_{\rm max}$, though. The magnetic field on scales larger than the Larmor radius is perceived by a charged particle as a quasi-homogeneous component that locally introduces a preferred direction of propagation [29]. A suitable parameter can be defined as ratio of the Larmor radius to $\lambda_{\rm max}$,

$$P = 10\pi \frac{r_{\rm L}}{\lambda_{\rm max}} \simeq 3.4 \left(\frac{R}{\rm PV}\right) \left(\frac{B_{\rm rms}}{\mu\rm G}\right)^{-1} \left(\frac{\lambda_{\rm max}}{10\ \rm pc}\right)^{-1} . \tag{3.1}$$

We present results for 4 cases whose parameters are summarized in Table 1. We consider only one specific field configuration here. Otherwise, the anisotropy signals would average out if we considered more than one field configuration. The parameter values are computed for a magnetic-field strength typical for interstellar space.

In Figure 2 we show the arrival distribution of the particles on the surface of the target sphere, obtained with the parameters for the cases 2 and 3 from Table 1. The turbulent magnetic field generates statistically significant anisotropic structures in the arrival distribution, which is represented as relative intensity $I_{\rm pixel}/I_0$ in units of the isotropic flux, I_0. Note that the simulation volume is much smaller than the cosmic-ray halo of the Galaxy, and so the amplitude of anisotropy is much larger in the simulation than it is in reality. Both the pattern and amplitude of the arrival distribution depend on $\lambda_{\rm max}$ or, equivalent to that, on the rigidity of the test particles, since particle ensembles

with the same parameter P show a similar propagation behaviour. Note, however, that the value of $\lambda_{\rm mfp}$ scales with the Larmor radius, $r_{\rm L}$. Hence, the observed energy dependence of the cosmic-ray anisotropy measured in the TeV-PeV range [6, 16] might be caused by the local turbulent magnetic field.

Second, in contrast to earlier studies [23], in which a global dipole moment is assumed, we show that it is not necessary to assume such a global dipole moment or any other initial large-scale distribution to generate small-scale anisotropies in the vicinity of Earth. Instead, our results suggest a natural generation of small-scale structures in the anisotropy even for the case of an initial isotropic particle distribution, implying that anisotropy is created *ex nihilo*. This issue is not a contradiction to Liouville's theorem, since the particles can leave the system in our forward-tracking method. Less than 1% of the particles launched on the injection sphere can hit the target sphere, and the launch positions of these particles are not equally distributed on the injection sphere, suggesting a correlation between the local escape probability and the likelihood to arrive at Earth. Thus, our method of forward-tracking reveals particle escape as important effect, whose contribution to the anisotropy should not be underestimated.

The pattern of the arrival distribution varies somewhat with the actual field realization, but its statistical properties are well defined by the parameter P. If $P \gtrsim 1$, the charged particles do not feel a coherent structure in the turbulent magnetic field anymore. In this case, the investigation of individual particle trajectories only shows the scattering events, but no helical motion. Thus, the arrival distribution of particles fulfilling $P > 1$ is affected only by the particle scattering off magnetic turbulence, resulting in small-scale and medium-scale anisotropies, as can be seen in the arrival distribution in the top left panel of Figure 2. In the same figure, we plot beneath the anisotropy patterns the mean angle between the line of sight and the magnetic field, $|\langle\cos\theta\rangle|$, where we averaged over 1–6 target radii. The bottom panels of Figure 2 demonstrate that for $P \gtrsim 1$ the local magnetic-field direction does not seem to correlate with the anisotropy patterns presented in the top panels of the same figure.

If the condition $P \ll 1$ is fulfilled, the distance covered by the relativistic particle within one gyro time, $2\pi\Omega^{-1}$, is much smaller than the coherence length of the turbulent magnetic field, and the charged particles can easily follow the magnetic-field lines. The trajectories of individual particles clearly show the characteristic helical motion. Hence, the turbulent magnetic field acts like a local homogeneous background field for these particles, giving rise to a preferred propagation direction. Our case 4 is designed to be in this limit. A strong dipole component in the arrival distribution that can be seen in Figure 3, and a comparison with the local magnetic-field within $1-6$ target radii shows a correlation between radial magnetic-field orientation and this dipole-like structure.

As additional check of the reliability of our results, we also tested twice larger radii for the injection sphere and outer boundary, respectively, implying much more computational efforts due to the larger propagation volume. Therefore, we restrict ourselves to a particle ensemble with fewer particles and do not consider the target spheres with radius halved. In these simulations, the statistical fluctuations are $\sim 7.2\,\%$ and $\sim 8.3\,\%$ for case 2 and 3, respectively. Nevertheless, the maps of the arrival distribution already start showing the same pattern of the anisotropy, and particle escape through the outer boundary is even more significant. Hence, our results remain valid even if we consider a larger propagation volume. Moreover, by considering larger injections spheres with

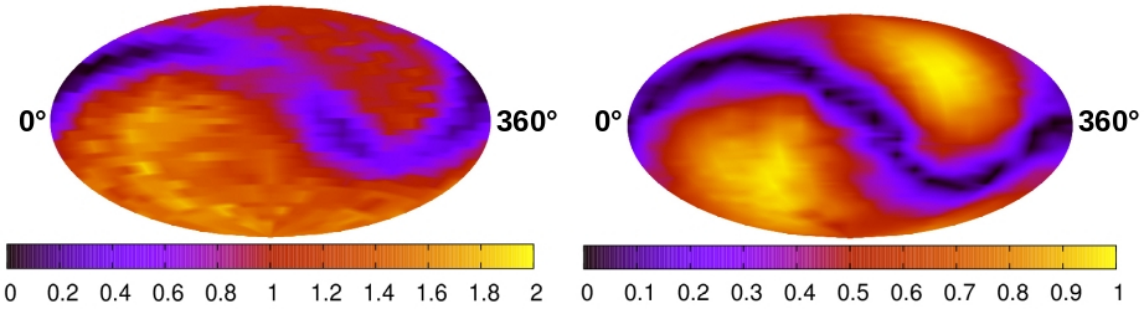

Figure 3: Anisotropy pattern (left panel) and average magnetic-field direction in the vicinity of the target sphere (right panel) for case 4.

the corresponding larger outer boundaries, we also show that the local magnetic turbulence within a few particle mean free paths indeed determines the arrival distribution on the target sphere.

We then also tested dynamical turbulence by imposing a constant phase velocity of waves. The resulting electric fluctuation should lead to momentum diffusion, but the final spread in momenta was found small even for a wave speed $v_\phi = 1000$ kms^{-1}. More interesting is that the magnetic-field model becomes oscillatory, and small-scale fluctuation are scrambled during the simulation. Small-scale anisotropy was still observed, albeit with slightly smaller amplitude than in the case of static turbulence, which suggests that the anisotropy is driven by magnetic-field structures on scales that are not scrambled. As for $v_\phi = 1000$ kms^{-1} scrambling will be effective up to a few pc (in the units of Table 1), commensurate with the scattering mean free path, a strong correlation with the very local magnetic field would not be expected.

4. Conclusions

We performed forward-tracing test-particle simulations of the propagation of relativistic charged particles in isotropic magnetic turbulence. Our main conclusion is that the arrival distribution obtained on the surface of a small target sphere is affected by the local turbulent magnetic field as well as by particle escape from the system. Related to cosmic rays, our results support the notion that the observed cosmic-ray anisotropy in the TeV-PeV energy range results from the structure of the turbulent magnetic field within a few cosmic-ray scattering lengths from Earth. However, we also account for escape, which renders Liouville's theorem not applicable and particle backtracing inappropriate. We find that an initial dipole is not needed to explain any anisotropic structure, since it is created *ex nihilo*.

Acknowledgements: Part of this work was supported by the Helmholtz Alliance for Astro particle Physics HAP funded by the Initiative and Networking Fund of the Helmholtz Association.

References

[1] M. Amenomori, S. Ayabe, S. W. Cui, et al., ApJL 626, (2005) L29.

[2] M. Amenomori, S. Ayabe, X. J. Bi, et al., Science 314, (2006) 439.

[3] G. Guillian, J. Hosaka, K. Ishihara, et al., PRL 75, (2007) 062003.

[4] A. A. Abdo, B. Allen, T. Aune, et al., PRL 101, (2008) 221101.

[5] A. A. Abdo, B. T. Allen, T. Aune, et al., ApJ 698, (2009) 2121.

[6] M. Aglietta, V. V. Alekseenko, B. Alessandro, et al., ApJL 692, (2009) L130.

[7] B. Bartoli, P. Bernardini, X. J. Bi, et al., PRD 88, (2013) 082001.

[8] A. U. Abeysekara, R. Alfaro, C. Alvarez, et al., ApJ 796, (2014) 108.

[9] R. Abbasi, Y. Abdou, T. Abu-Zayyad, et al., ApJL 718, (2010) L194.

[10] R. Abbasi, Y. Abdou, T. Abu-Zayyad, et al., ApJ 740, (2011) 16.

[11] A. D. Erlykin & A. W. Wolfendale, Astrop. Phys. 25, (2006) 183.

[12] P. Blasi & E. Amato, JCAP 1, (2012) 011.

[13] M. Pohl & D. Eichler, ApJ 766, (2013) 4.

[14] A. D. Erlykin & A. W. Wolfendale, JCAP 4, (2013) 006.

[15] R. Kumar & D. Eichler, ApJ 785, (2014) 129.

[16] R. Abbasi, Y. Abdou, T. Abu-Zayyad, et al.,ApJ 746, (2012) 33.

[17] M. G. Aartsen, R. Abbasi, Y. Abdou, et al., ApJ 765, (2013) 55.

[18] M. Salvati & B. Sacco, A&A 485, (2008) 527.

[19] L. O. Drury & F. A. Aharonian, Astrop. Phys. 29, (2008) 420.

[20] M. A. Malkov, P. H. Diamond, L. O'C. Drury, & R. Z. Sagdeev, ApJ 721, (2010) 750.

[21] A. Lazarian & P. Desiati, ApJ 722, (2010) 188.

[22] P. Desiati & A. Lazarian, ApJ 762, (2013) 44.

[23] G. Giacinti & G. Sigl, PRL 109, (2012) 071101.

[24] M. Ahlers, PRL 112, (2014) 021101.

[25] J. Giacalone & J. R. Jokipii, ApJL 430, (1994) L137.

[26] J. Giacalone & J. R. Jokipii, ApJ 520, (1999) 204.

[27] R. C. Tautz & A. Dosch, Phys. Pl. 20, (2013) 022302.

[28] K. M. Górski, E. Hivon, A. J. Banday, et al., ApJ 622, (2005) 759

[29] E. Battaner, J. Castellano, M. Masip, ApJ 799, (2015) 157